Original Paper

Landslides
DOI 10.1007/s10346-026-02724-x
Received: 27 June 2025
Accepted: 19 February 2026

Sarah Johnson · Yichuan Zhu · Jason M. Dortch · William C. Haneberg

Quantifying landslide strain localization phenomena using tensor analysis of multi-temporal lidar data

Abstract A fundamental understanding of landslide evolution requires characterizing how deformation localizes within the sliding mass, as these non-homogeneous zones provide crucial insights into how destabilization initiates, failure surfaces develop, and the overall kinematic behavior evolves. While traditional analysis often assumes uniform movement, this study presents a methodology to quantify intricate patterns of surface deformation at a fine scale, allowing for the direct analysis of localization behavior. By applying strain tensor analysis to high-resolution displacement fields derived from multi-temporal Uncrewed Aerial Vehicle-Light Detection and Ranging (UAV-lidar) and Structure from Motion (SfM) surveys, we compute the divergence, gradient, and curl fields for two distinct landslides: one translational and one rotational. This approach quantifies volumetric changes, translational strain, and rotational components, revealing unique kinematic signatures for each landslide type. The translational slide is characterized by alternating expansion-contraction patterns along its dip-line, whereas the rotational slide exhibits clear, separate bands of head subsidence and toe expansion, coupled with non-uniform rotation along the strike. This detailed characterization of strain localization provides direct observational evidence of the fundamental mechanisms governing landslide behavior. It offers a more nuanced, mechanistic understanding that advances the interpretation of slope instability, providing a stronger physical basis for hazard assessment and risk management.

Keywords Landslide kinematics · Strain localization · UAV-lidar · Hazard assessment · Strain tensor · Surface deformation

Introduction

Landslides, among the most destructive geological hazards globally, account for thousands of casualties, severe infrastructure damage, and enormous economic losses every year worldwide (Kirschbaum et al. 2010; Froude and Petley 2018). In the USA, landslides occur in all states and inhabited US territories, causing billions of dollars in damage and averaging 25–50 fatalities each year (Crawford et al. 2021; Khabiri et al. 2023). Understanding landslide's kinematics and failure mechanisms is paramount for effective hazard assessment, mitigation, and early warning (Crawford et al. 2022). Traditionally, the study of a landslide's evolution has often relied on constitutive studies that assume a homogeneous body of media, where instability occurs when shear forces globally exceed the material's frictional and cohesive resistance (Fredlund and Krahn 1977; Cooper et al. 1998). This approach typically models soil or rock as a continuum, which permits a constitutive description that averages material responses over a representative volume (Zienkiewicz 1971; Cascini et al. 2010; Cuomo et al. 2012). However, this macroscopic view faces challenges when considering the geomechanics of granular materials at finer scales. At the meso- or micro-scale, the evolution of landslides is intrinsically linked to the development and progression of strain localizations, encompassing phenomena such as localized translation, rotation, shearing, and volumetric changes within the deforming mass (Borja et al. 2013; Zhu and Medina-Cetina 2022; Medina-Cetina et al. 2022). We will show in this study that investigating localization phenomena is crucial as they can directly govern the fundamental failure mechanisms from initiation to catastrophic failure (Morcioni et al. 2022; Marmoni et al. 2023).

The analysis of strain fields, derived from observed displacements, historically has been primarily applied in crustal deformation research. For instance, Frank (1966) deduced shear strain components associated with earthquakes from repeated triangulation surveys. Bibby (1975) analyzed shear strain under the assumption that strain changes linearly with time, using triangulation data from a series of surveys around the Wairau Fault in the Marlborough District of New Zealand. Cohen and Cook (1978) described analytical and numerical methods to determine crustal strain rate based on measurements from the spaceborne geodynamics ranging system, and Dermanis and Livieratos (1983) presented strain tensors in various spatial contexts relevant to Earth deformations. Shen et al. (1996) introduced a modified least-squares method to interpolate strain rates using discretized geodetic measurements, and Pietrantonio and Riguzzi (2004) provided three-dimensional strain tensor estimation from Global Positioning System (GPS) observations.

More recently, the principles of strain analysis have been increasingly applied to characterize the kinematics of landslides, making use of advancements in remote sensing technologies capable of providing detailed surface displacement data (Baum et al. 1988; Baum and Fleming 1991; Keaton and Gailing 2004; Delacourt et al. 2007; Mazza et al. 2023). For example, Teza et al. (2008) computed strain fields from multi-temporal displacement data acquired via Terrestrial Laser Scanning (TLS) for landslides in the Italian Alps, which demonstrated the potential to recognize different kinematic behaviors and reveal discontinuities. Baroň et al. (2017) applied paleostress analysis of fault-slip data to reconstruct the stress field of an active mudslide in Pechgraben, Austria. The results were compared with airborne laser scanning digital terrain models that revealed the dynamics and superficial displacements of the moving mass before and after the survey. Guerriero et al. (2017) employed an integrated approach combining surface mapping, GPS monitoring, lidar surveys, and geophysical investigations to

analyze sediment discharge variability and kinematic behavior of the Mount Pizzuto earth flow in southern Italy. While such studies explore the utility of strain analysis in landslide characterization, a critical gap persists in developing robust methodologies to directly process dense, raw surface displacement data into comprehensive, high-fidelity strain localization fields. There is a pressing need not only for improved techniques to derive these detailed strain localization fields but, more importantly, to systematically utilize these fields as direct observational evidence to illuminate the fundamental failure mechanisms of landslides. This involves moving beyond simply identifying localized features and instead using the spatially and temporally resolved strain patterns to understand how instabilities initiate at the material scale, how shear zones develop and propagate, and how these localized processes coalesce and interact to drive the progressive failure and ultimate collapse of the slope. Such mechanistic understanding is essential for improving hazard assessment models and designing more effective mitigation strategies. By directly linking observable strain patterns to underlying failure processes, practitioners can better predict the extent of slope failures, identify critical zones requiring intervention, and optimize the placement of monitoring instrumentation and stabilization measures.

Here, we present a methodology for deriving and interpreting detailed strain localization fields from high-resolution, multi-temporal lidar survey data that advances the understanding of landslide evolution. Specifically, this work seeks to (1) compute and analyze strain localization fields from these displacement data to quantify volumetric changes, translational and extensional/compressional behavior, and rotational components within active landslides; (2) characterize and compare the distinct non-homogeneous deformational patterns and kinematic signatures associated with both translational (Taylor Mill) and rotational (Highland Pike) landslide types; and (3) utilize the observed spatio-temporal evolution of these strain localization fields as direct evidence to infer the fundamental processes driving landslide development, such as the initiation and propagation of internal deformation zones and the development of complex failure kinematics. By focusing on the detailed spatial and temporal evolution of strain, this work seeks to provide new insights into the complex mechanics governing the behavior of different landslide types.

Study location

The Cincinnati, Ohio, and Northern Kentucky region (Fig. 1) is home to numerous slow-moving landslides that threaten infrastructure (Mirus et al. 2020; Johnson et al. 2023). For example, in 2019, several landslides along a major road cost over $17 million USD and took 2 years to remediate (City of Cincinnati Transportation and Engineering 2019). Landslides in the region include slow-moving translational debris slides that form in the colluvium that mantles the steep slopes along the Ohio River and tributary valleys (Varnes 1978; Fleming and Johnson 1994), and deeper, slow-moving rotational slides that occur in thick colluvium, glacial deposits, or anthropogenic fill (Baum and Johnson 1996). The colluvium involved in many landslides is derived from weathered shale and limestone of the Ordovician Kope Formation (Fig. 1) which is composed of weak illitic shale that readily slakes when exposed to water (Koralegedara and Maynard 2017). Translational debris slides in the region are typically < 2 m thick, while rotational slides may exceed 15 m in depth. Both may be active for decades, moving at rates ranging from a few mm per year to a meter or more per year, typically moving during the wetter spring months (Fleming and Johnson 1994). The Taylor Mill landslide (39.034234, −84.512587) is a translational debris slide that has been active since at least 2003 and has repeatedly damaged a roadway leading to an apartment complex (Fig. 1) (Johnson et al. 2023). Attempts to mitigate the slide have included regrading the slope, rebuilding part of the roadway, and excavating the toe of the slide. The rotational slide along Highland Pike (39.044714, −84.540806) formed in colluvium and anthropogenic fill that was placed on the slope between 1994 and 2000 as part of a road rerouting project. The slide has been active since at least 2004 and has damaged a sewer line and the park and walking trail. The landslide is approximately 310 m wide and has had vertical displacements of more than 6 m.

Methods

Acquisition of multi-temporal landslide displacement fields

To analyze the deformation processes of the two slow-moving landslides, we used multi-temporal digital elevation models (DEMs) capturing elevation changes between 2019 and 2022 (Table 1). These DEMs were derived from a combination of Uncrewed Aerial Vehicle (UAV) Structure from Motion (SfM) surveys and UAV-lidar surveys. These datasets were employed to compute displacement patterns, which formed the basis for subsequent strain analysis.

Digital aerial photographs for the SfM surveys were acquired in 2019, 2020, and 2022 during leaf-off conditions using DJI Mavic Phantom 2 and Mavic Pro UAVs. Both landslides have low vegetation and uncut grass, and we assumed that vegetation differences between years were negligible (Haneberg 2008). Flight planning was performed ensuring 75% forward overlap and 70% side overlap between images, and the same flight plan was repeated for each survey. The photographs were processed into point clouds using Agisoft Metashape (Agisoft 2025). Georeferencing was achieved using 19 readily identifiable ground control points (GCPs) located in stable areas outside the landslide boundaries. These GCPs, such as sewer grates and the base of light poles, were selected due to their visibility in the KYAPED 2012 aerial photographs, and corresponding elevations were obtained from the 2012 state-wide lidar-derived DEM. The total residual error for the GCPs was less than 0.02 m (Johnson et al. 2023). Ground point classification within Metashape was performed using the "Classify Ground Points" tool, with parameters set to a maximum angle of 15°, a maximum distance of 0.5 m. The resulting SfM point clouds exhibited an average ground return density of 3.6 ± 1.9 points per 0.1 m^2 bin.

The UAV-lidar data were acquired in December 2020 using a Matrice 600 Pro UAV equipped with a Yellowscan Surveyor lidar system. The Yellowscan Surveyor uses a Velodyne VLP-16 lidar scanner with a 903 nm wavelength and has an accuracy of 5 cm. Post-processing of the UAV-lidar data involved referencing to local Continuously Operating Reference Station (CORS) data to enhance positional accuracy. Point elevations were further refined through strip adjustment, and points were classified into ground and non-ground returns using Yellowscan CloudStation software. The UAV-lidar ground point cloud had an average density of 3.3 ± 2.4 points per 0.1 m^2 bin.

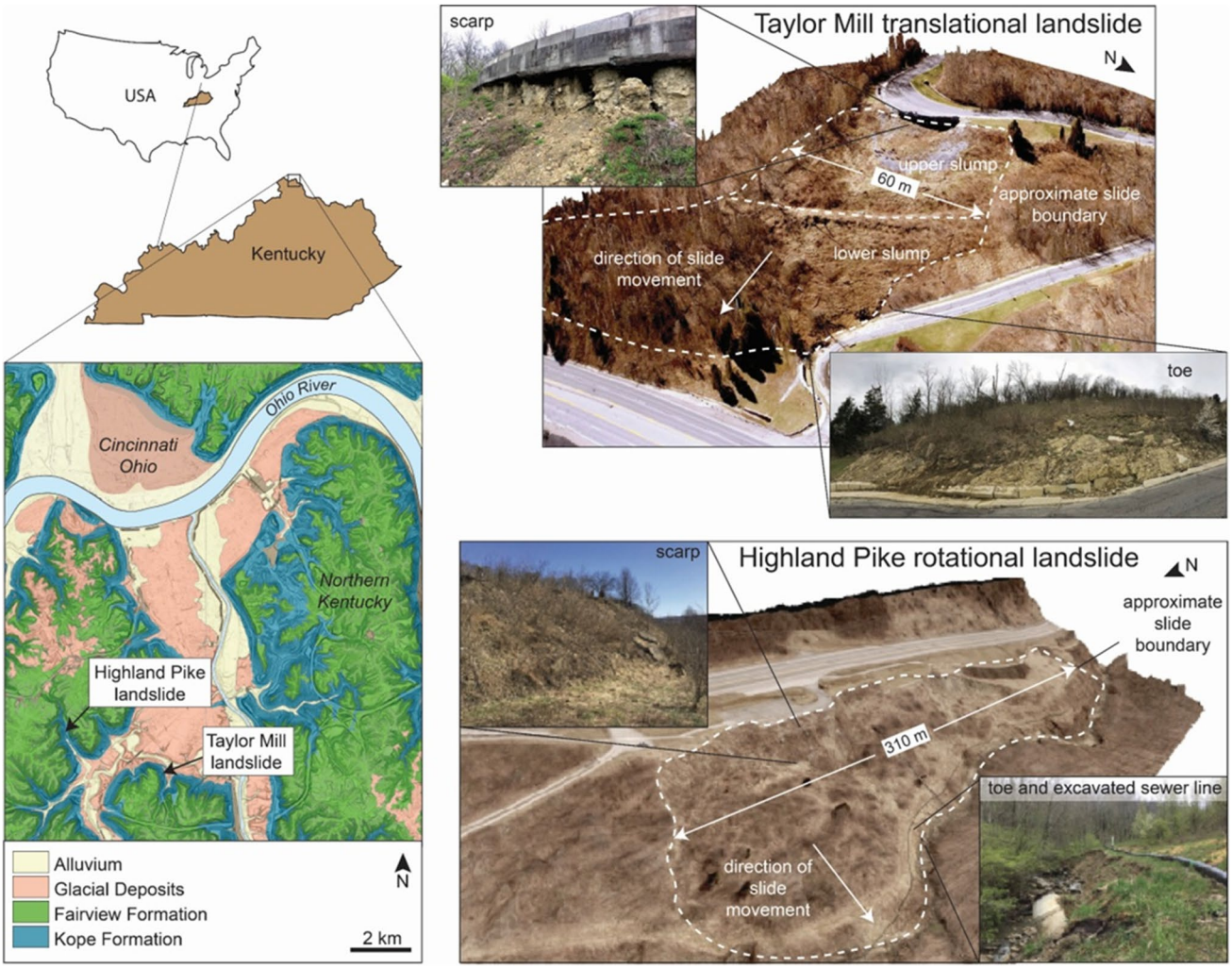

Fig. 1 Geological map of Northern Kentucky showing the locations of the Taylor Mill translational debris slide (*39.034234*, *−84.512587*) and the Highland Pike rotational landslide (*39.044714°*, *−84.540806°*), and oblique photo of the Taylor Mill translational landslide and the Highland Pike rotational landslide

Table 1 Methods and dates of data acquisition

Landslide	Date	Method	Referenced in paper as
Taylor Mill	March 11, 2019	UAV-SfM	2019
Taylor Mill	March 3, 2020	UAV-SfM	2020
Taylor Mill	December 15, 2020	UAV-lidar	2021
Taylor Mill	March 29, 2022	UAV-SfM	2022
Highland Pike	March 11, 2019	UAV-SfM	2019
Highland Pike	March 3, 2020	UAV-SfM	2020
Highland Pike	December 15, 2020	UAV-lidar	2021

Point clouds were processed in ArcGIS (ESRI 2025) to generate 0.1 m cell size DEMs. The natural neighbor interpolation method was employed to fill any voids in the data. A consistent area of interest (AOI) was used to define the processing extent for all DEMs, ensuring grid alignment. This step was crucial to prevent slight variations in grid origin that would otherwise occur if each DEM was based solely on the southeasternmost point of its respective point cloud. All datasets were projected in UTM Zone 16 N, EPSG 26916. Errors due to elevation bias and tilt between surveys were corrected using an analysis of elevation difference errors in areas of no change outside of the landslides, which is described fully in Johnson et al. (2023). While geomorphological change can be quantified via grid-based (DEM) or point cloud comparisons, we used gridded DEMs as calculating DEM differences is easily accomplished using map algebra within GIS software and has a long history of successful application in change detection studies (e.g., Qin et al. 2016; Okyay et al. 2019). Differentiation, as is required to compute the tensor elements, amplifies noise, and the minor smoothing required to produce a gridded DEM may produce

cleaner and more easily interpretable vector fields. Furthermore, it is inherent to the point cloud classification process that some details of the ground surface will be lost, or if filtering is not aggressive enough, be obscured by non-ground points. This is another reason to prefer a slightly smoothed interpolated and regularly gridded surface as the basis for subsequent differentiation to obtain the tensor components.

Horizontal displacement for each combination of DEMs was estimated using COSI-Corr image correlation software (Leprince et al. 2007; Ayoub et al. 2009, 2017). COSI-Corr works by first generating accurate ground control points for each image, which are then used to build an orthorectification model. This model allows an accurate orthorectification and co-registration of the two images and provides the horizontal ground displacement vectors between them. The frequency correlator engine, with an initial window size of 32 by 32 pixels (3.2 m on the ground), a final window size of 8 by 8 pixels (0.8 m on the ground), and a step size of 4 pixels, was used to produce a vector field map with a grid spacing of 2 m. There are between 712 and 944 horizontal displacement values on the landslide itself for the Taylor Mill landslide, and 4584 on the Highland Pike landslide. To produce the vector field, elevations corresponding to the initial points were derived from the earlier DEM (ex. 2019), and the elevations of the displaced points were derived from a later DEM (ex. 2020).

Coordinate transformation

Haneberg (2007) introduced a workflow to produce directional rock surface profiles from three-dimensional photogrammetric or laser scanner point clouds. The dip-line, strike-line, and normal to the joint plane form an orthogonal coordinate system that simplifies the calculation of profile roughness. We adopted the same approach in this work, enabling us to obtain the directional gradient and strain fields of the slope being studied. Assuming a point cloud $\mathbf{p} = (x_i, y_i, z_i)^T$ is defined in Cartesian coordinate system, the best-fit plane passing through the centroid of the point cloud is the eigenvector corresponding to the smallest eigenvalue of the covariance matrix.

$$\mathbf{\Sigma} = \begin{bmatrix} \sum_{i=1}^{N}(x_i-\overline{x})^2 & \sum_{i=1}^{N}(x_i-\overline{x})(y_i-\overline{y}) & \sum_{i=1}^{N}(x_i-\overline{x})(z_i-\overline{z}) \\ \sum_{i=1}^{N}(x_i-\overline{x})(y_i-\overline{y}) & \sum_{i=1}^{N}(y_i-\overline{y})^2 & \sum_{i=1}^{N}(x_i-\overline{x})(z_i-\overline{z}) \\ \sum_{i=1}^{N}(x_i-\overline{x})(y_i-\overline{y}) & \sum_{i=1}^{N}(y_i-\overline{y})(z_i-\overline{z}) & \sum_{i=1}^{N}(z_i-\overline{z})^2 \end{bmatrix} \quad (1)$$

In which the $\overline{x}$, $\overline{y}$, and $\overline{z}$ are the arithmetic mean of point cloud $\mathbf{p}$ along each axis direction, and together, they represent the centroid of the point cloud. The eigenvectors $\mathbf{n} = \{\mathbf{n}_x, \mathbf{n}_y, \mathbf{n}_z\}$ of covariance matrix $\mathbf{\Sigma}$ correspond to the new orthogonal basis that maximizes the variance of the data, defining the best-fit plane of $\mathbf{p}$ when viewed in vector space.

To apply the transformation, we can compute the dot product between the normalized coordinates of point cloud $\mathbf{p}$ and the eigenvectors $\mathbf{n} = \{\mathbf{n}_x, \mathbf{n}_y, \mathbf{n}_z\}$. The center of the fitting plane is Easting = 715,330.5, Northing = 432,348.3, and Elevation = 178.5. Figure 2 presents the best-fit plane of the points cloud along with transformed orientation axes that expand (x' and y') and perpendicular (z') to the best-fit plane for the Taylor Mill landslide.

Gradient tensor

We used strain tensors in Euclidean space to quantify the evolution of the two landslides at the site scale. Similar methodology has been successfully applied to investigate the localization effects that occurred in a series of triaxial sand specimens in laboratory studies (Zhu and Medina-Cetina 2022; Zhu et al. 2022, 2026). In the three-dimensional space, the gradient of a vector field $\mathbf{V}$ is a second-order tensor $\mathbf{F} = \nabla \otimes \mathbf{V}$ composed of nine strain components representing the translational or rotational deformation tendencies of the local area affected by the vector field V.

$$grad\,\mathbf{V} = \nabla \otimes \mathbf{V} = \begin{bmatrix} F_{11} & F_{12} & F_{13} \\ F_{21} & F_{22} & F_{23} \\ F_{31} & F_{32} & F_{33} \end{bmatrix} = \begin{bmatrix} \frac{\partial V_x}{\partial x} & \frac{\partial V_y}{\partial x} & \frac{\partial V_z}{\partial x} \\ \frac{\partial V_x}{\partial y} & \frac{\partial V_y}{\partial y} & \frac{\partial V_z}{\partial y} \\ \frac{\partial V_x}{\partial z} & \frac{\partial V_y}{\partial z} & \frac{\partial V_z}{\partial z} \end{bmatrix} \quad (2)$$

The sum of diagonal terms in Eq. 2 is the divergence indicating the total magnitude of volumetric contraction or expansion of a local area. That is,

$$div\,\mathbf{V} = \nabla \cdot \mathbf{V} = \frac{\partial V_x}{\partial x} + \frac{\partial V_y}{\partial y} + \frac{\partial V_z}{\partial z} \quad (3)$$

Figure 3 illustrates the application of gradient, divergence, and curl to landslide behavior. Where the flow of material slows or converges, the divergence is negative and represents a volumetric contraction of the local area. Areas such as a landslide scarp, the head of a rotational slide, or where excavation has occurred would be expected to have a negative divergence (Fig. 3a and b). Where material in a landslide expands or the flow increases, the divergence is positive and is an area of gain. Areas such as landslide toes would be expected to have positive divergence values (Fig. 3a and b). The curl field shows where there is a rotation about an axis. While this can be calculated for any axis, for a landslide, the rotation would be expected around the Y axis which is analogous to the strike of the slope. A positive curl is a clockwise rotation about Y, as viewed looking to the North, while a negative curl is a counterclockwise rotation about Y (Fig. 3c). Within a landslide, alternating regions of positive and negative curl might be expected where there are smaller-scale slumps and deformation within the landslide. The gradient field shows strain parallel to the dip of the slope (the X direction) and normal to the slope (the Z direction) (Fig. 3d). A positive gradient in the Z direction might be expected for a landslide toe, while a negative gradient in the Z direction would be expected at the head of a rotational slide or landslide scarp. The gradient field in the X direction might be expected to show areas of shortening and lengthening within the body of the landslide.

The difference between every two off-diagonal terms in Eq. 1 gives each component of curl representing local rotational behavior with respect to each axis of (x, y, z), as shown in Eq. 4.

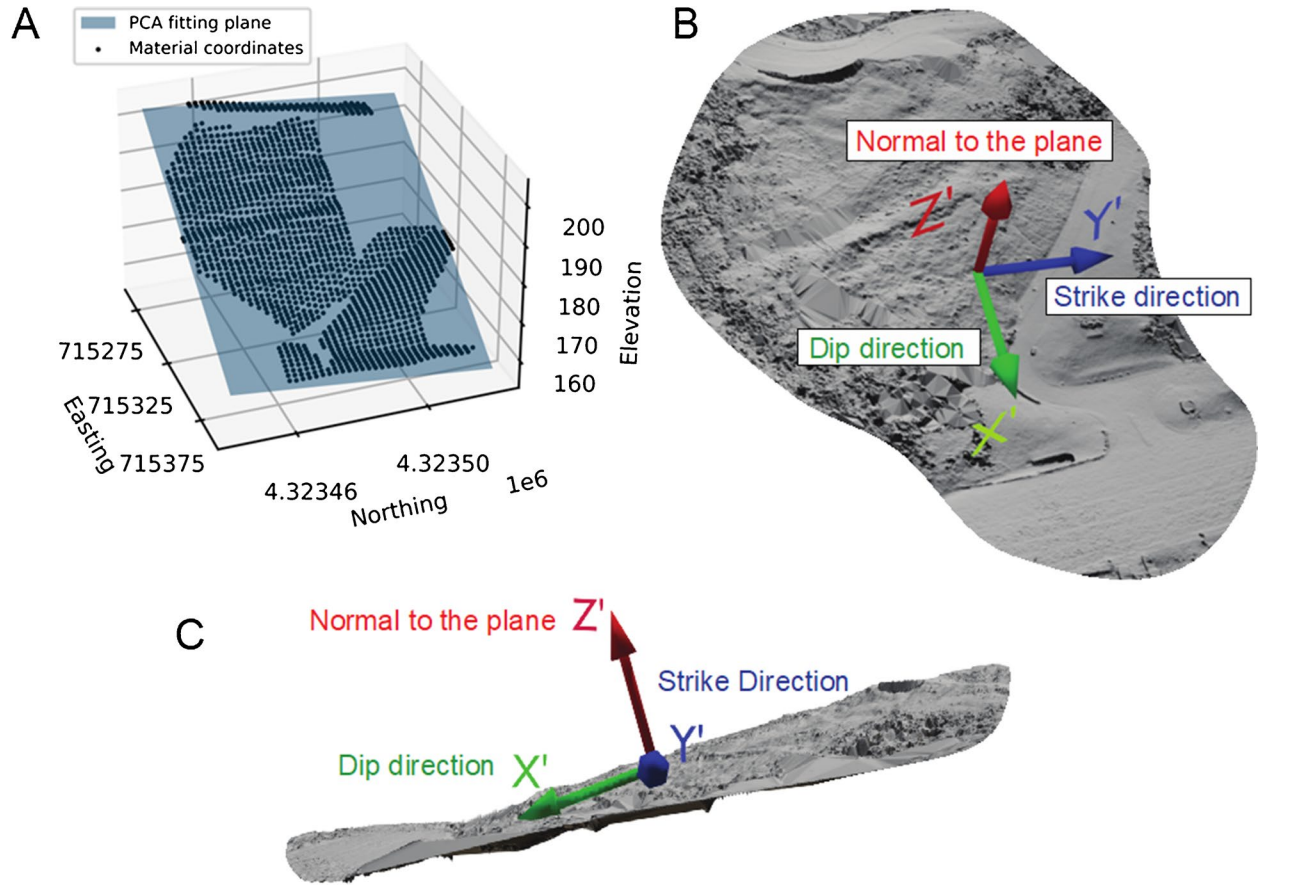

Fig. 2 **A** Points cloud (Taylor landslide) and best-fit plane according to principal component analysis (PCA). **B** Hillshade of Taylor landslide and transformed orientation axes. **C** View along the strike-line of the slope

$$
\begin{aligned}
curl\,\mathbf{V} &= \nabla \times \mathbf{V} = (curl\,\mathbf{V})_x + (curl\,\mathbf{V})_y + (curl\,\mathbf{V})_z \\
&= \left(\frac{\partial V_z}{\partial y} - \frac{\partial V_y}{\partial z}\right)\hat{i} + \left(\frac{\partial V_x}{\partial z} - \frac{\partial V_z}{\partial x}\right)\hat{j} + \left(\frac{\partial V_y}{\partial x} - \frac{\partial V_x}{\partial y}\right)\hat{k} \\
&= \begin{bmatrix} \frac{\partial V_z}{\partial y} - \frac{\partial V_y}{\partial z} \\ \frac{\partial V_x}{\partial z} - \frac{\partial V_z}{\partial x} \\ \frac{\partial V_y}{\partial x} - \frac{\partial V_x}{\partial y} \end{bmatrix}
\end{aligned} \tag{4}
$$

where $\mathbf{i}$, $\mathbf{j}$, and $\mathbf{k}$ are the unit vectors for the x, y, and z axes.

Results

Displacement fields

Figure 4 presents the displacement field of the Taylor Mill landslide observed between 2021 and 2022. Significant movements are identified behind the head of the lower slump and around its toe area. This pattern suggests that, at the current stage, the landslide is primarily driven by the movement of the lower slump. This activity also induces translational behavior at the base of the upper slump. Figure 5 shows the displacement field of the Highland Pike landslide between 2020 and 2021. In clear distinction to the Taylor Mill landslide, the slump movement at Highland Pike exhibits a distinct rotational pattern. This is characterized by subsidence in the upper slump and uplift in the lower slump. Movement in the transitional zone between the upper and lower slump blocks is less significant compared to the head and toe areas.

Translational landslide—Taylor Mill case

Divergence fields *div* **V**

To calculate the gradient fields for the Taylor Mill landslide, multitemporal DEMs from consecutive years (2019 to 2020, 2020 to 2021, and 2021 to 2022) were used to compute the corresponding displacement fields. Subsequently, the divergence of the kinematic field, denoted as *div* **V**, was computed for each processed displacement dataset. The divergence represents the net magnitude of volumetric change, indicating areas of material sink (volumetric compaction) or source (volumetric expansion) within a local area.

Figure 6 illustrates the divergence field *div* **V** for the Taylor Mill landslide across each annual window. The area presented for analysis is relatively small compared to the entire landslide surface due to the exclusion of regions affected by construction activities and tall vegetation (Johnson et al. 2023, Fig. 6). The results consistently show that significant volumetric behavior across all observed year windows was concentrated in the lower slump of the landslide, divided by a scarp feature appearing in the middle of the slope.

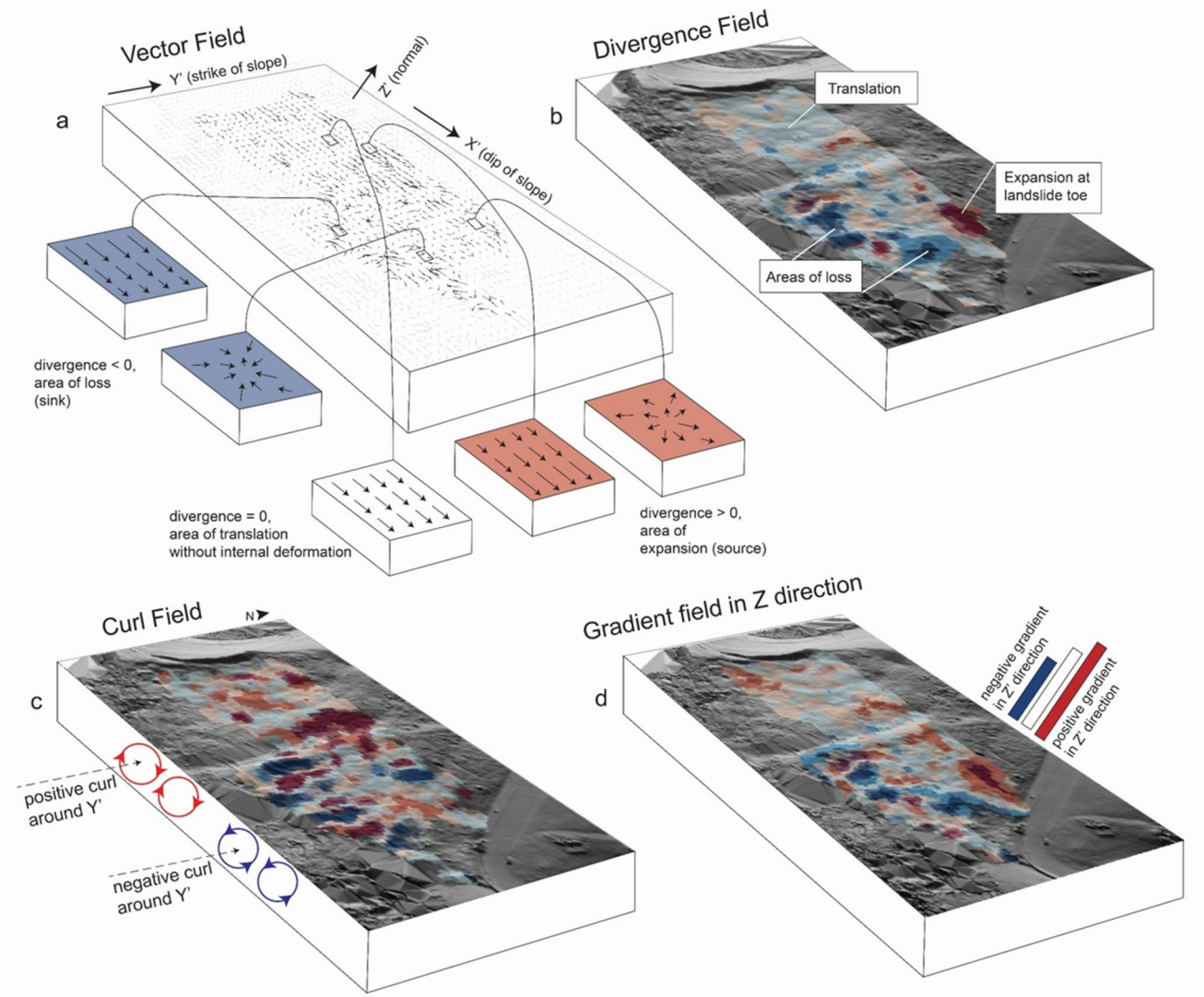

Fig. 3 **a** Vectors that represent positive and negative divergence. **b** The resulting divergence map for the Taylor Mill landslide. **c** An example of the curl field for the Taylor Mill landslide and **d** an example of the gradient field in the Z direction

During the 2019 to 2020 period, the volumetric behavior around the toe was complex, as the landslide toe was partially excavated in 2019 to clear the roadway. From 2020 to 2021, the toe area predominantly exhibited volumetric expansion, suggesting volumetric expansion in this zone following the excavation. In the 2021 to 2022 period, the volumetric change displayed an alternating pattern of expansion and compaction along the dip-line of the slope. This observation suggests that the translational movement of the landslide induced a localized, alternating volumetric expansion-compaction behavior, which contrasts with conventional, simplified assumptions of homogeneous deformational patterns (Fredlund & Krahn 1977; Zienkiewicz 1971).

Gradient fields F_{11} and F_{33}

Figure 7 presents the gradient field component F_{11} along the X' axis, which is aligned with the dip-line direction of the slope, indicating translational behavior. These results corroborate the findings illustrated by the volumetric behaviors shown in Fig. 6. The partial excavation of the landslide toe, as described in the previous section, resulted in complex slope movement, which is reflected as a relatively variable pattern in the F_{11} gradient field for the timeframe between 2019 and 2020. For the 2021 to 2022 window, an alternating expanding-contracting pattern is observed along the dip-line of the slope, clearly exhibiting the essential translational characteristics of the landslide. Figure 8 presents the gradient field component F_{33} along the Z′ direction (normal to the slope plane), indicating subsidence or uplift behavior. The patterns of F_{33} are closely related to the volumetric behaviors presented in Fig. 6. Moreover, the gradient field F_{33} shows greater magnitudes in the lower slump compared to the upper slump, indicating that the lower portion was more active during this deformation stage (2019–2022)—a finding that is corroborated by the displacement vector map in Fig. 4.

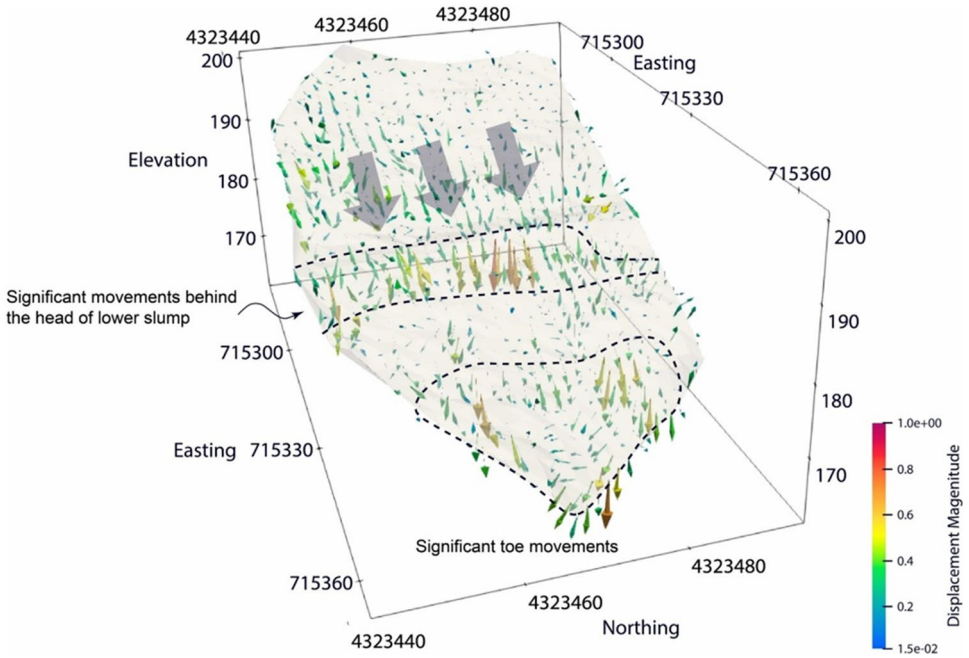

Fig. 4 The displacement field of Taylor Mill landslide between the years 2021 and 2022

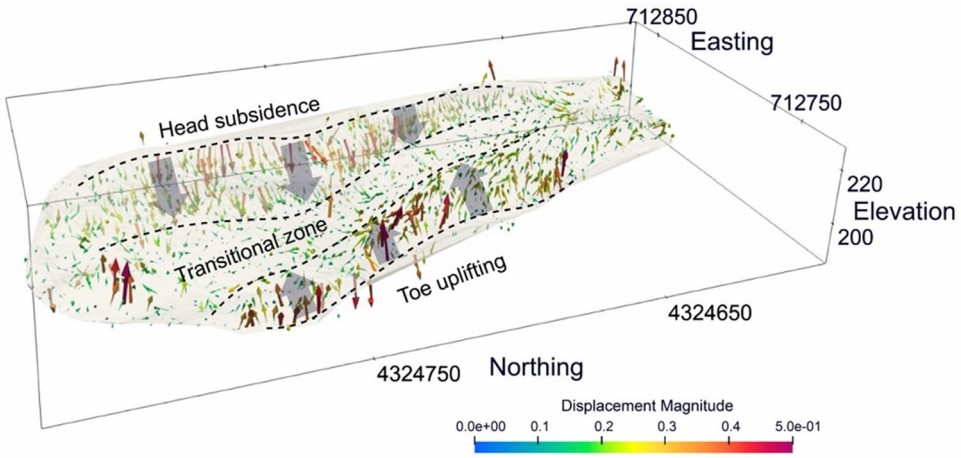

Fig. 5 The displacement field of Highland Pike landslide between the years 2020 and 2021

Curl fields $(Curl)_{Y'}$

Figure 9 presents the curl fields along the Y′ direction, $(Curl)_{Y'}$, which indicates rotational behavior about an axis aligned with the strike-line for the Taylor Mill landslide. Due to significant subsidence occurring along the scarp zone in the middle of the slope, a general clockwise rotation is observed in this local area across all annual monitoring periods. Furthermore, relatively significant rotation is also evident in the upper half of the slope during the 2021 to 2022 period. This latter rotation may be attributed to the subsidence of the lower half of the landslide (as indicated by the divergence field in Fig. 6c), which creates accommodation space for the translational movement along the dip-line, as shown in Fig. 4.

Rotational landslide—Highland Pike case

Divergence fields *div* **V**

A similar set of gradient field analyses was conducted for the Highland Pike landslide, which is characterized as a rotational type. Figure 10 presents the divergence fields derived from the sampled displacement fields for the 2019 to 2020 and 2020 to 2021 periods. The results indicate that the rotational behavior of the slump block may have been initiated by toe movement between 2019 and 2020. During this period, the toe movement exhibited wider coverage and greater magnitude compared to the subsidence observed at

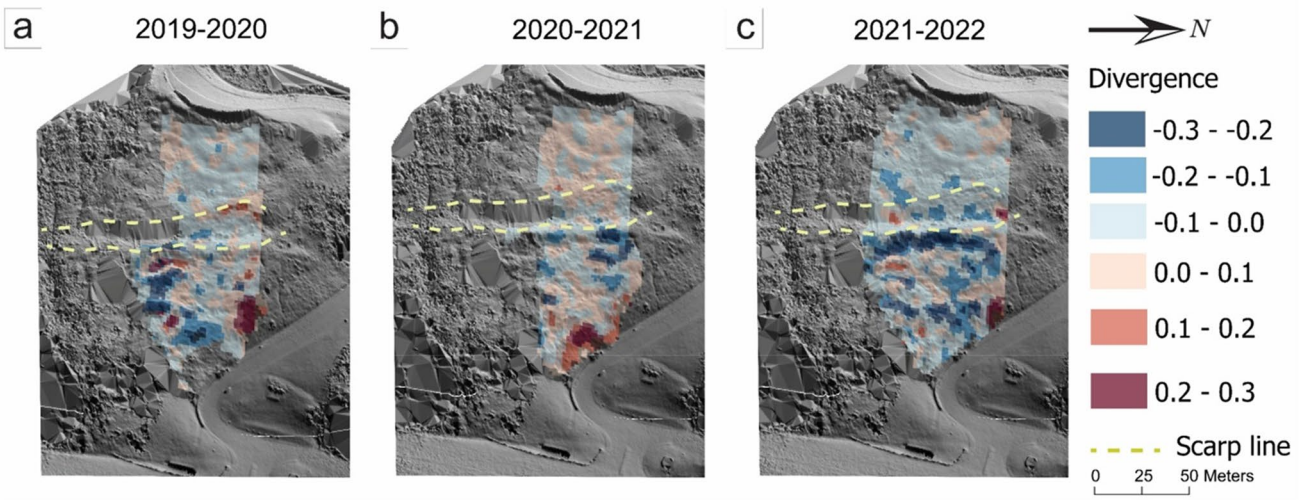

Fig. 6 The divergence fields of Taylor landslide, showing volumetric behaviors during the year windows 2019 to 2020 (**a**), 2020 to 2021 (**b**), and 2021 to 2022 (**c**)

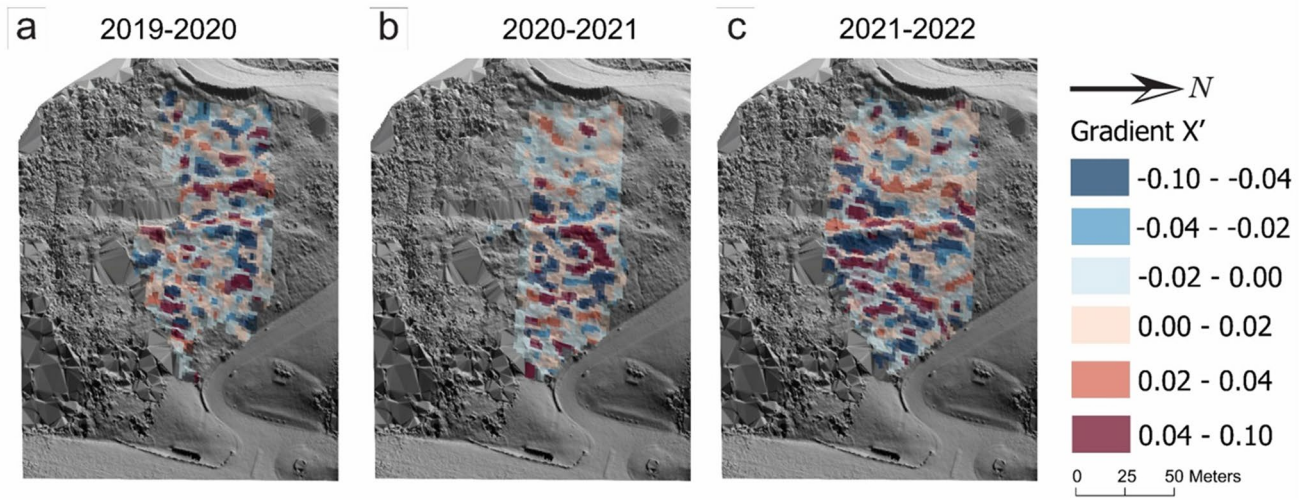

Fig. 7 The gradient fields along X′ direction F_{11} for Taylor landslide, showing translational behavior along dip-line direction during the year windows 2019 to 2020 (**a**), 2020 to 2021 (**b**), and 2021 to 2022 (**c**)

the head of the slope. From 2020 to 2021, the localized divergence behavior, previously more concentrated (Fig. 10a), bifurcated into two distinct banding areas: one characterized by compaction at the top of the slump and another by expansion at the bottom. The magnitude of these changes also suggests an acceleration in straining, which may warrant concern regarding potential failure in the near future.

Gradient fields F_{11} and F_{33}

Figures 11 and 12 illustrate the gradient field components F_{11} (along the dip-line direction) and F_{33} (normal to the slope plane), respectively, for the Highland Pike landslide. Figure 11 reveals a clear alternating pattern of expansion and contraction along the dip direction of the slump. During the 2019 to 2020 period, significant movement was concentrated on the northern part of the slope. However, from 2020 to 2021, this localization pattern spread across all active landslide zones.

Regarding the gradient fields F_{33} along the normal-to-plane direction (Fig. 12), a tendency for downward movement (subsidence) in the upper half of the slope and upward movement (uplift) in the lower half is apparent, consistent with the rotational behavior of the slope. A notable observation is that the gradient fields along Z′ are localized between 2019 and 2020 but exhibit a more uniform distribution between 2020 and 2021.

Curl fields $(Curl)_{Y'}$

The curl fields $(Curl)_{Y'}$ along the strike-line direction (Y′ axis) describe a general clockwise rotation about an axis aligned with

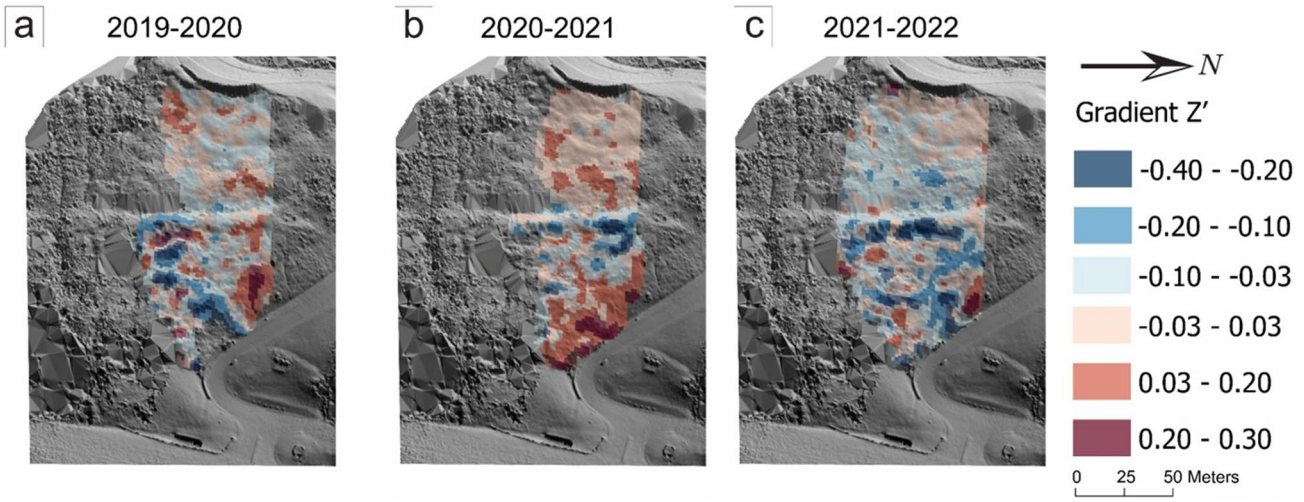

Fig. 8 The gradient fields along Z′ direction F_{33} for Taylor landslide, showing behavior along normal to plane direction during the year windows 2019 to 2020 (**a**), 2020 to 2021 (**b**), and 2021 to 2022 (**c**)

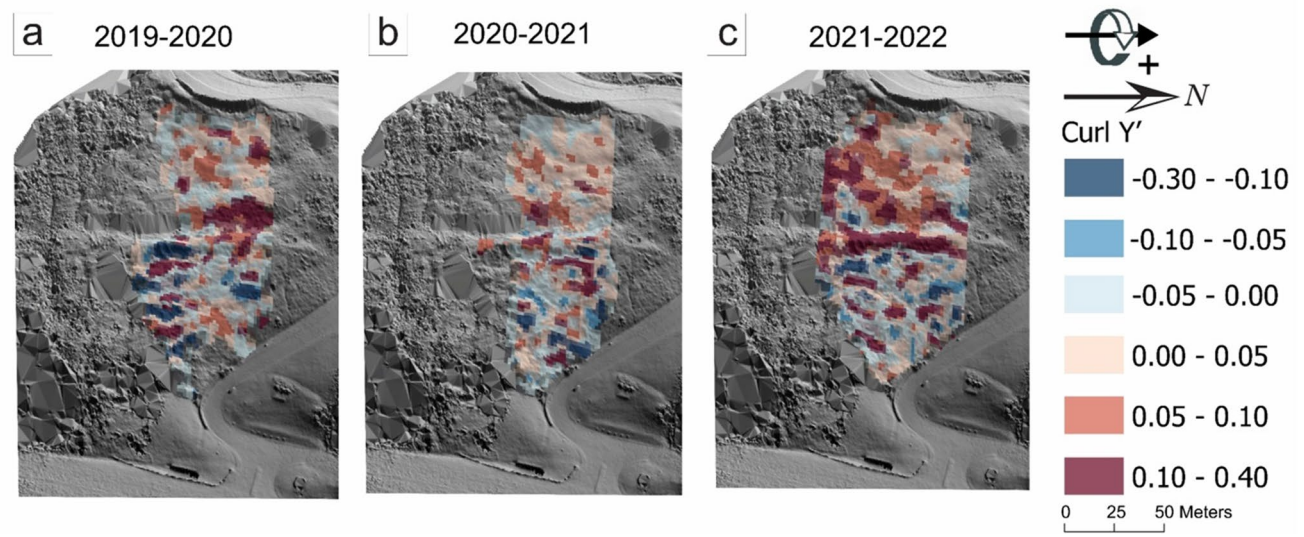

Fig. 9 The curl fields along Y′ direction $(Curl)_{Y'}$ for Taylor landslide, showing rotational behavior along Y′ axis during the year windows 2019 to 2020 (**a**), 2020 to 2021 (**b**), and 2021 to 2022 (**c**)

the northerly direction for the Highland Pike landslide (Fig. 13). When compared to the $(Curl)_{Y'}$ for the Taylor Mill landslide (Fig. 9), the rotational behavior in the Highland Pike case is more uniform and extends over a larger area.

Kinematic signatures in landslide evolution

Figure 14 presents the kinematic signatures interpreted as evolving force chains (i.e., load-bearing networks within the slope material) within the scarp zone of the Taylor Mill landslide. Figure 14e defines the spatial domain for the kinematic plots illustrated in Fig. 14a–d. These subplots (Fig. 14a–d) reveal a distinct spatial sequence of localization patterns. The initial significant localization observed is local expansion along the dip-line direction. This is followed by rotation about the strike-line axis. Subsequently, compaction along the normal-to-plane direction occurs, coupled with overall volumetric compaction. Further down-slope, a counter-clockwise rotation about the strike-line axis is observed. This phase is accompanied by slight or negligible expansion along the normal-to-plane direction, and a similar trend is noted in the overall volumetric behavior.

Figure 14f and g offers a hypothetical illustration of this interpreted process. The down-slope movement along the dip-line is thought to cause force chain buckling behind the head of the slump, inducing a clockwise rotation in the local area. Subsequent compression along the normal-to-plane direction leads to local volumetric compaction. The point of maximum volumetric compaction

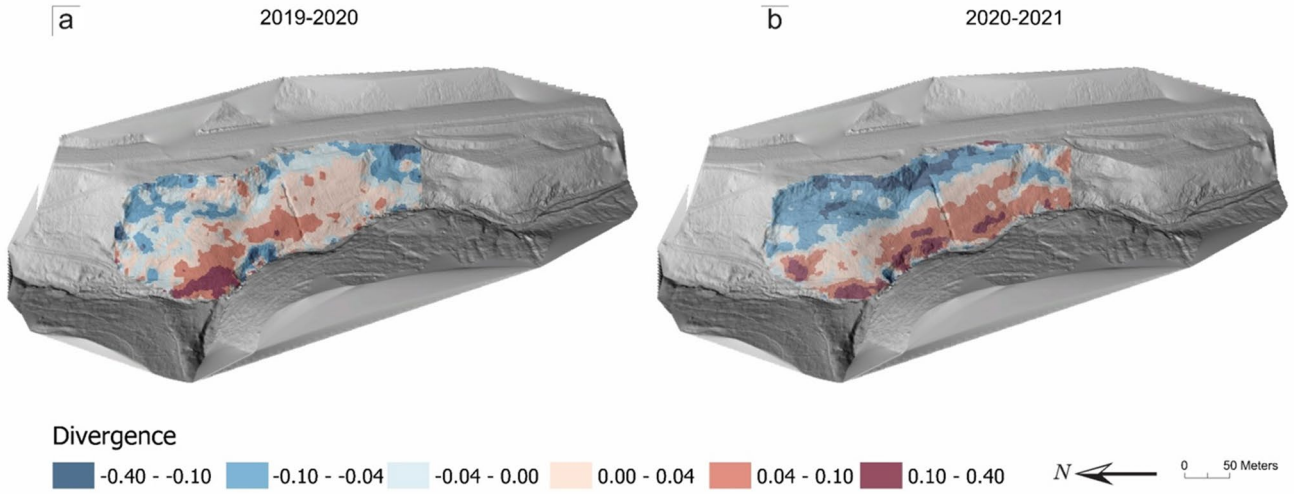

Fig. 10 The divergence fields of Highland Pike landslide, showing volumetric behaviors during the year windows 2019 to 2020 (**a**) and 2020 to 2021 (**b**)

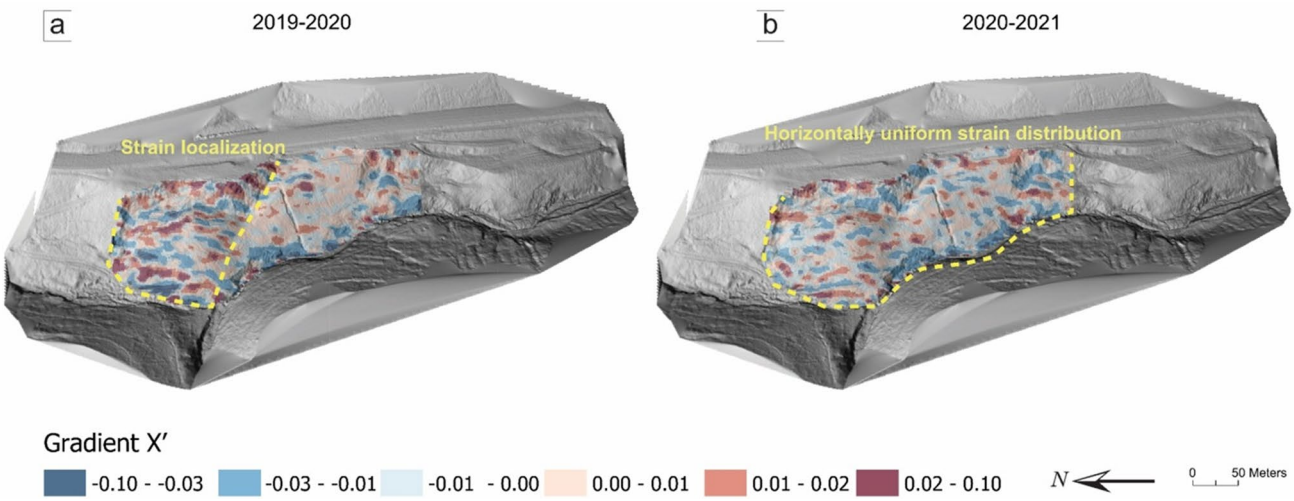

Fig. 11 The gradient fields along X′ direction F_{11} for Highland Pike landslide, showing translational behavior along strike-line direction during the year windows 2019 to 2020 (**a**) and 2020 to 2021 (**b**)

appears to be associated with an area of neutral rotation, where the formation of strong force chains is inferred. Following this zone of maximum compaction, a "snow plowing" effect is hypothesized to cause the local area to rotate counter-clockwise. In this distal area, compaction is observed along the dip-line direction, while expansion occurs along the normal-to-plane direction, resulting in a net volumetric change that is slight to negligible expansion.

Non-homogeneous deformation is also evident in rotational landslides, as exemplified by the Highland Pike case in this study. Figure 15a displays a swath profile analysis of the Highland Pike landslide, focusing on the divergence field. The analysis utilized the *PyOSP* intelligent swath profile tool (Zhu et al. 2021), which automatically truncates swath lines along the irregular boundaries of the slope under investigation. The study region was classified into three zones (A, B, and C) based on the variability of interquartile ranges (IQR) of divergence, as depicted in Fig. 15a. Zone B exhibits a clearly more significant IQR variability compared to zones A and C. This suggests that zone B was more kinematically active, reflected by more substantial volumetric changes. Further evaluation involved analyzing the cross-swath profiles for each zone. Figure 15c–e presents density scatter plots (where color intensity indicates spatial density, with red representing high density and blue representing low density) of divergence values within each swath produced by *PyOSP*, overlain by the mean divergence for each profile. Between 2019 and 2020, significant toe movement was observed in zone C. Conversely, from 2020 to 2021, zone C showed minimal toe movement but significant subsidence at the head, indicating a new area of energy mobilization. Zone B exhibited a general whole-slope rotational pattern, characterized by uplift at its upper part and subsidence

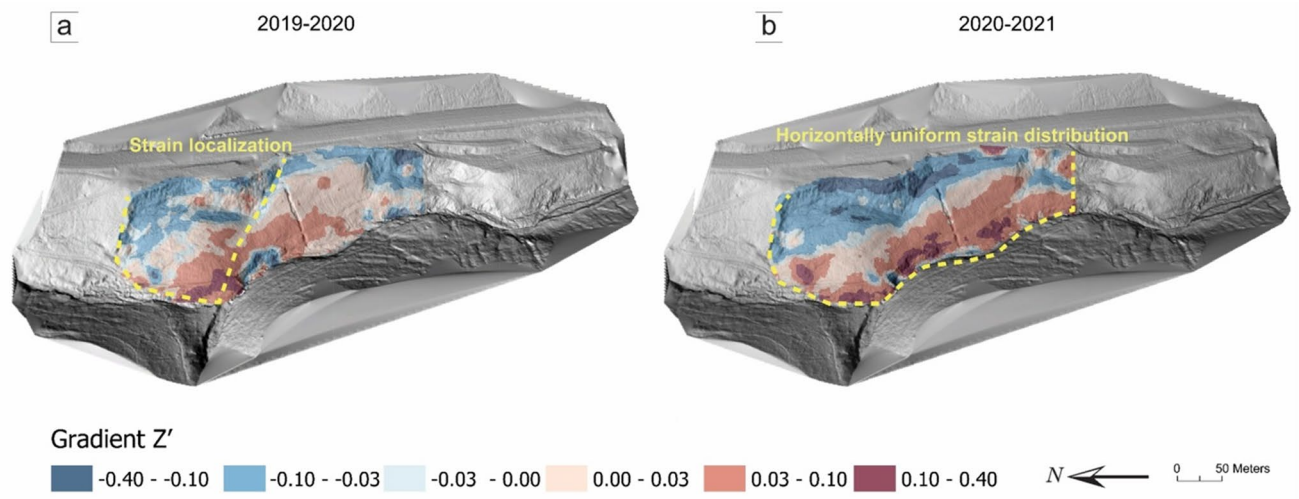

Fig. 12 The gradient fields along Z′ direction F_{33} for Highland Pike landslide, showing translational behavior along dip-line direction during the year windows 2019 to 2020 (**a**) and 2020 to 2021 (**b**)

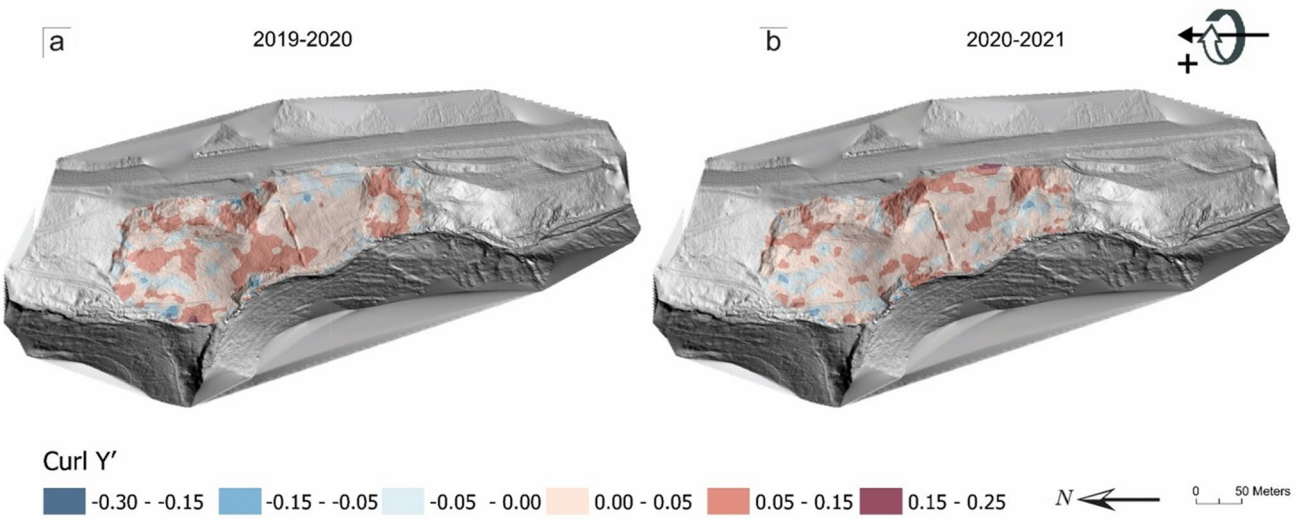

Fig. 13 The curl fields along Y′ direction $(Curl)_{Y'}$ for Highland Pike landslide, showing rotational behavior along Y′ axis during the year windows 2019 to 2020 (**a**) and 2020 to 2021 (**b**)

at its head. Zone A displayed uplift in its upper region with no significant movement at its head. This pattern indicates that the rotational behavior is not uniformly distributed along the strike-line of the slope. Instead, an alternating sequence of dominant head movement, then general slope rotation, and then dominant toe movement is observed across different zones of the landslide.

Discussion

We used SfM- and lidar-enabled landslide monitoring data to understand the effects of strain localization on landslide development. While a significant body of research has addressed the constitutive behavior, travel characteristics, or general descriptive analyses of landslides (e.g., review articles such as Delacourt et al. 2007; Hungr et al. 2005; and Varnes 1978), there is not much literature focused on comprehensive understanding of fundamental, quantitative, and fine-scale landslide development mechanisms. We have demonstrated that the application of UAV-lidar surveys coupled with engineering strain tensor analysis can detail non-homogeneous deformational patterns and elucidate their influence on different types of landslides at various stages of deformation. This understanding of localized strain provides crucial insights into how destabilization initiates and accumulates, how failure surfaces develop, and how the overall kinematic behavior of a landslide evolves, moving beyond simplified homogeneous assumptions.

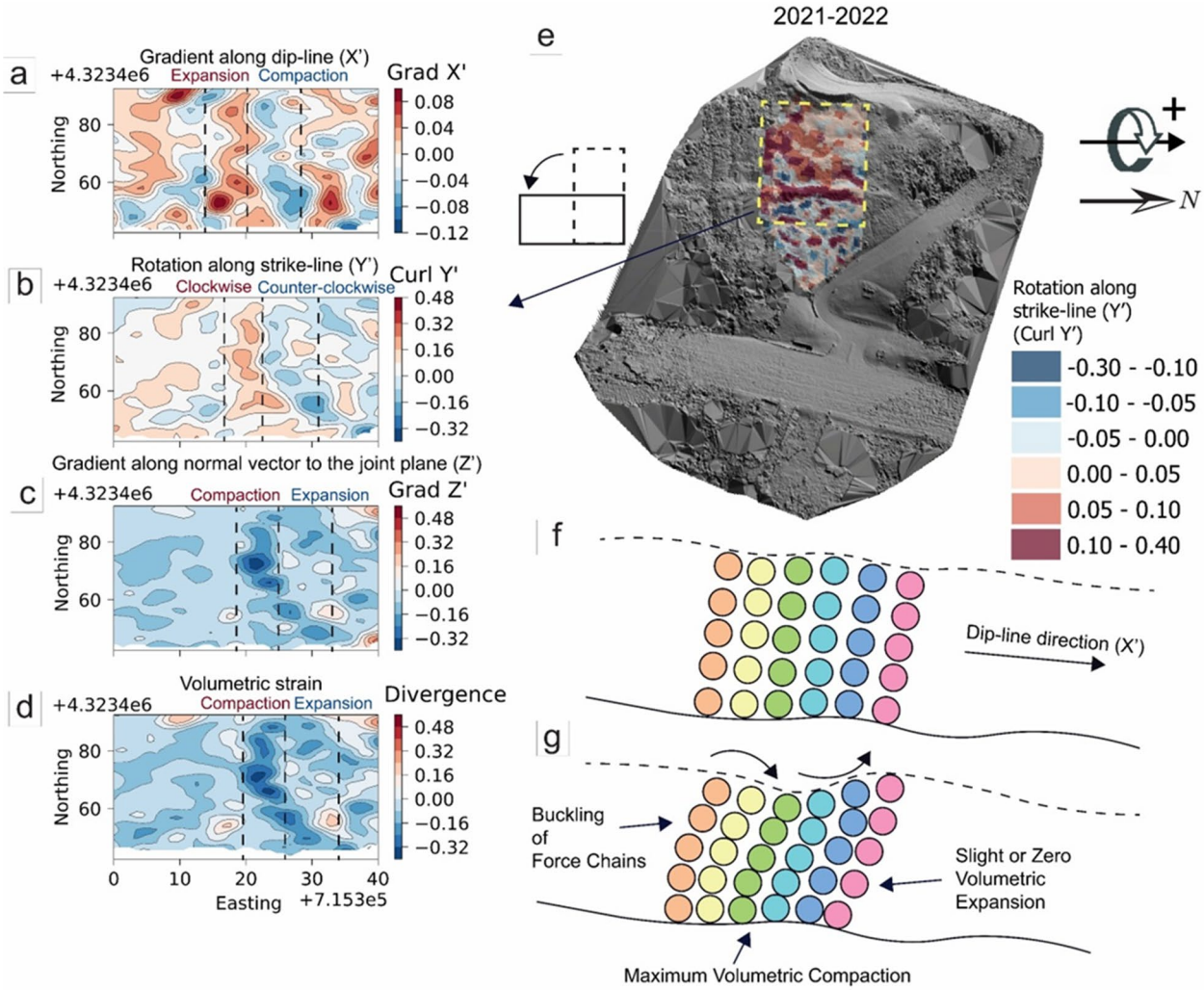

Fig. 14 **a** The gradient field along the dip-line direction F_{11}. **b** The curl fields along Y′ direction $(Curl)_{Y'}$. **c** The gradient field along normal to plane direction F_{33}. **d** The divergence field. **e** The curl field along Y′ direction $(Curl)_{Y'}$ for Taylor Mill landslide 2021–2022. **f** The hypothetical illustration of initial arrangement of force chains perpendicular to the dip-line direction. **g** The hypothetical illustration of rearrangement of force chains after the deformation

A truly fundamental understanding of landslide development necessitates monitoring data that spans the entire lifespan of a landslide: from initiation at the meso- or micro-scale, through stages of strain localization and bifurcation, to eventual catastrophic failure. Current monitoring techniques each possess distinct advantages and limitations (Delacourt et al. 2007; Mazza et al. 2023). For instance, traditional geodetic methods like GPS or in situ instrumentation can provide accurate, often continuous, monitoring data for specific points on a landslide, but their spatial resolution is typically coarse, potentially missing localized phenomena (Malet et al. 2002; Pietrantonio and Riguzzi 2004). Interferometric Synthetic Aperture Radar (InSAR) techniques offer wide spatial coverage and potentially short revisit times (Schulz et al. 2017) but can be limited by decorrelation in vegetated areas, geometric distortions in steep terrain, and atmospheric effects, particularly for moderate to small or rapidly moving slides. Image-based methods (e.g., optical image correlation, SfM photogrammetry) and point cloud analyses (e.g., from TLS or lidar) can provide high-resolution data; however, individual surveys may have limited spatial coverage or temporal frequency, potentially overlooking intermittent strain signatures critical to understanding landslide phase transitions. Ideally, an integrated monitoring strategy could offer a more robust solution for landslide hazard assessment and management. For example, combining landslide inventories, imagery, and InSAR techniques can help identify landslide-prone areas. Constitutive or machine learning models could then be employed for landslide forecasting and early warning, while terrestrial or UAV-lidar surveys can capture high-resolution landslide movement series for detailed health monitoring and methodology validation. Such an integrated approach could generate synergies, taking advantage of the strengths of each individual technique.

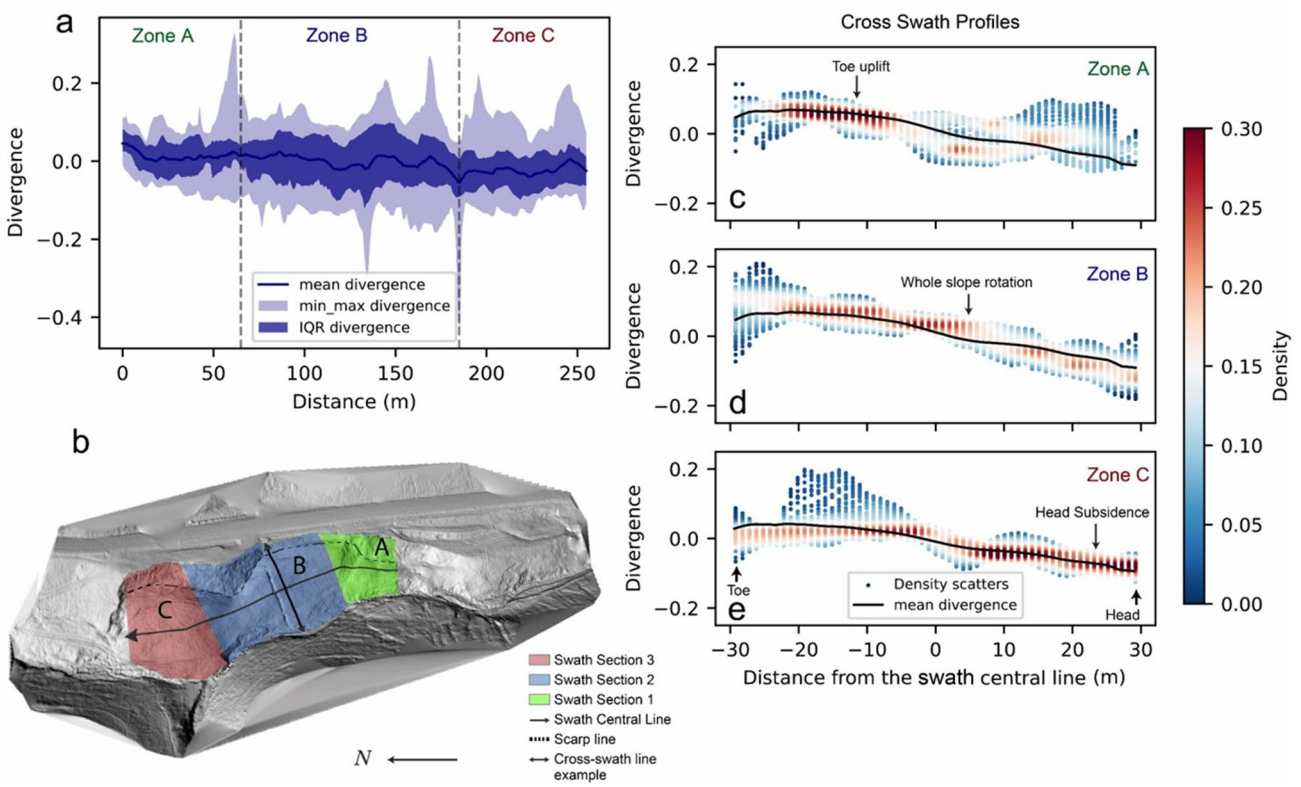

Fig. 15 **a** Swath profile of Highland Pike landslide. **b** Swath zones A, B, and C that are classified based on interquartile range in **a**. **c** Density scatters and mean divergence of cross swath profile for zone A. **d** Density scatters and mean divergence of cross swath profile for zone B. **e** Density scatters and mean divergence of cross swath profile for zone C

It is also emphasized that observed surface deformation may only be a manifestation of prior or ongoing internal deformation processes. Factors such as internal deformation, pore water pressure fluctuations, and spatio-temporal variability in geotechnical properties all exert significant influence on landslide development (Haneberg and Gökce 1994). Traditional geotechnical and hydrological instrumentation (e.g., inclinometers, piezometers, rain gauges) and geophysical methods remain irreplaceable for capturing these subsurface conditions and triggers. Their importance is particularly acute in heavily populated areas or where landslides threaten critical infrastructure, such as hospitals, emergency services, and energy facilities.

The strain localization characterization presented here can potentially contribute to landslide hazard assessment in several fundamental ways. The derived strain tensor fields, including divergence, gradient, and curl components, can serve as quantitative indicators of landslide evolutionary phases, revealing the initiation and propagation of deformation zones that precede catastrophic failure. The distinct kinematic signatures we identify for translational versus rotational landslides (alternating expansion-contraction patterns versus separated bands of subsidence and expansion) establish mechanistic relationships between strain localization patterns and failure modes. With additional temporal sensing data, this approach could potentially reveal more localization patterns and inform early warning systems by providing signature kinematic elements that indicate critical phase transitions. By demonstrating how strain accumulates and localizes both temporally and spatially, our methodology addresses a critical gap in current risk assessment approaches, which predominantly rely on static susceptibility models that neither incorporate time-dependent strain evolution nor integrate real-time monitoring data.

On the site scale, our methodology can provide applications for slope engineering and mitigation design. The detailed strain localization fields can guide optimal placement of monitoring instrumentation by identifying zones where deformation concentrates and where failure initiation is most likely. The established relationships between surface strain patterns and basal slip surface geometry can inform targeted subsurface investigation strategies, reducing costs while improving characterization. Furthermore, the identification of extension versus compression zones enables strategic positioning of mitigation measures: drainage systems can be prioritized in extensional areas where enhanced permeability facilitates water infiltration, while reinforcement elements can be concentrated in compressional zones experiencing stress accumulation. Our future research aims to deepen the study of strain localization phenomena by fusing data from diverse sampling methods and integrating these observations at a system level. The rapid advancements in Artificial Intelligence (AI) frameworks, including explainable AI (XAI), generative AI, and multi-modal AI, offer promising avenues for integrating this fundamental knowledge of strain localization with other geo-environmental variables. This could lead to the development of new AI paradigms for more robust landslide

hazard assessment (Al-Najjar et al. 2023; Alqadhi et al. 2024; Akosah et al. 2024). The overarching goal is to transform landslide analysis from a predominantly static, susceptibility-focused practice into a dynamic, process-oriented science. This may foster a symbiotic relationship where machine learning predictions refine physical models, while physical laws and process understanding constrain generative AI scenarios. The ultimate objective, to quantify "why," "when," and "where" landslides occur, complete with uncertainty-aware confidence intervals, will redefine landslide risk assessment and management, catalyzing a paradigm shift from reactive to proactive landslide science.

Conclusion

This study demonstrates the significant capability of employing high-resolution, multi-temporal lidar data, in conjunction with engineering strain tensor analysis, to investigate and characterize complex strain localization phenomena integral to landslide development. Through case studies of both translational (Taylor Mill) and rotational (Highland Pike) landslides, we have shown that this methodological approach allows for the quantification of non-homogeneous deformational patterns at a fine spatial and temporal scale.

For the Taylor Mill translational landslide, the analysis revealed that significant volumetric changes and associated strains were concentrated in the lower slump, with distinct alternating expansion-compaction patterns along the dip-line indicative of its translational nature, contrasting with simplified homogeneous deformation models. The study also highlighted how localized subsidence and uplift (gradient normal to the slope) dominated the net volumetric behavior and how rotational components (curl) near the scarp zone and upper slope were linked to the overall translational movement and accommodation of material. In the case of the Highland Pike rotational landslide, the strain analysis clearly depicted the characteristic head subsidence and toe uplift, with divergence fields showing an evolution from toe-initiated movement to distinct bands of compaction (head) and expansion (toe) that suggest accelerating strain. The non-uniform rotational behavior along the strike, with alternating zones of dominant head, general slope, and toe movement, was effectively captured by swath profile analysis of the divergence field, correlating with observed geomorphic features like scarp formation.

These findings underscore the critical importance of moving beyond displacement measurements alone to characterize localized strain for a more fundamental understanding of how damage initiates and accumulates, how internal shear zones and failure surfaces develop and propagate, and how the overall kinematic behavior of different landslide types evolves over time. While acknowledging the inherent limitations of current individual monitoring techniques and the ideal of capturing the entire landslide lifecycle from initiation to failure, this work demonstrates that detailed strain localization analysis can effectively differentiate failure mechanisms and reveal non-homogeneous deformation patterns that are obscured by displacement measurements alone. Ultimately, this research contributes to the broader scientific goal of transforming landslide hazard assessment from a reactive, often descriptive, practice into a proactive, predictive, and mechanistic science, thereby significantly enhancing future risk management capabilities.

Funding

This research did not receive any specific grant from funding agencies in the public, commercial, or not-for-profit sectors.

Data Availability

The Kentucky geologic map data used in this paper are freely available through the Kentucky Geological Survey website (http://kgs.uky.edu) as GIS-compatible files. The statewide lidar point cloud and hydro-corrected DEM files derived from the point cloud are freely available through the Kentucky From Above program website (http://kyfromabove.ky.gov). Any additional queries may be directed to the corresponding author.

Declarations

Competing interests The authors request that this manuscript not be sent to Dr. Xinli Hu at China University of Geosciences and Dr. Lu Cong at Shanxi University for review due to collaboration on related research topics.

References

Agisoft (2025) AgiSoft PhotoScan standard. Retrieved from http://www.agisoft.com/

Akosah S, Gratchev I, Kim D-H, Ohn S-Y (2024) Application of artificial intelligence and remote sensing for landslide detection and prediction: systematic review. Remote Sens 16:2947. https://doi.org/10.3390/rs16162947

Al-Najjar HAH, Pradhan B, Beydoun G et al (2023) A novel method using explainable artificial intelligence (XAI)-based Shapley Additive Explanations for spatial landslide prediction using Time-Series SAR dataset. Gondwana Res 123:107–124. https://doi.org/10.1016/j.gr.2022.08.004

Alqadhi S, Mallick J, Alkahtani M (2024) Integrated deep learning with explainable artificial intelligence for enhanced landslide management. Nat Hazards 120:1343–1365. https://doi.org/10.1007/s11069-023-06260-y

Ayoub F, Leprince S, Avouac J-P (2009) Co-registration and correlation of aerial photographs for ground deformation measurements. ISPRS J Photogramm Remote Sens 64:551–560. https://doi.org/10.1016/j.isprsjprs.2009.03.005

Ayoub F, Leprince S, Avouac J-P (2017) User's guide to COSI-CORR co-registration of optically sensed images and correlation. Calif Inst Technol 38:49

Baroň I, Kernstocková M, Melichar R (2017) Stress field reconstruction in an active mudslide. Geomorphology 289:170–178. https://doi.org/10.1016/j.geomorph.2017.04.020

Baum RL, Fleming RW (1991) Use of longitudinal strain in identifying driving and resisting elements of landslides. Geol Soc Am Bull 103:1121–1132. https://doi.org/10.1130/0016-7606(1991)103<1121:UOLSII>2.3.CO;2
Baum RL, Johnson AM (1996) Overview of landslide problems, research, and mitigation, Cincinnati, Ohio, area. US Government Printing Office, Washington, D.C
Baum RL, Johnson AM, Fleming RW (1988) Measurement of slope deformation using quadrilaterals. United States Geological Survey, p 23
Bibby HM (1975) Crustal strain from triangulation in Marlborough, New Zealand. Tectonophysics 29:529–540
Borja R, Song X, Rechenmacher A et al (2013) Shear band in sand with spatially varying density. J Mech Phys Solids 61:219–234. https://doi.org/10.1016/J.JMPS.2012.07.008
Cascini L, Cuomo S, Pastor M, Sorbino G (2010) Modeling of rainfall-induced shallow landslides of the flow-type. J Geotech Geoenviron Eng 136:85–98. https://doi.org/10.1061/(ASCE)GT.1943-5606.0000182
City of Cincinnati Transportation and Engineering (2019) 2019 Columbia Parkway landslide evaluation and report
Cohen SC, Cook GR (1978) Determining crustal strain rates with spaceborne geodynamics ranging system data. 1: baseline analysis
Cooper MR, Bromhead EN, Petley DJ, Grants DI (1998) The Selborne cutting stability experiment. Geotechnique 48:83–101. https://doi.org/10.1680/geot.1998.48.1.83
Crawford MM, Dortch JM, Koch HJ, Killen AA, Zhu J, Zhu Y, Bryson LS, Haneberg WC (2021) Using landslide-inventory mapping for a combined bagged-trees and logistic-regression approach to determining landslide susceptibility in eastern Kentucky, United States. Q J Eng Geol Hydrogeol 54(4). https://doi.org/10.1144/qjegh2020-177
Crawford MM, Dortch JM, Koch HJ et al (2022) Landslide risk assessment in Eastern Kentucky, USA: developing a regional scale, limited resource approach. Remote Sens 14:6246. https://doi.org/10.3390/rs14246246
Cuomo S, Prime N, Iannone A et al (2012) Large deformation FEMLIP drained analysis of a vertical cut. Acta Geotech. https://doi.org/10.1007/s11440-012-0179-2
Delacourt C, Allemand P, Berthier E et al (2007) Remote-sensing techniques for analysing landslide kinematics: a review. Bulletin de la Société Géologique de France 178:89–100. https://doi.org/10.2113/gssgfbull.178.2.89
Dermanis A, Livieratos E (1983) Applications of deformation analysis in geodesy and geodynamics. Rev Geophys 21:41–50
Environmental Systems Research Institute (Esri) (2025) ArcGIS pro. Redlands, CA. Retrieved from https://www.esri.com/en-us/arcgis/products/arcgis-pro
Fleming RW, Johnson AM (1994). Landslides in colluvium. US Government Printing Office, Washington, D.C
Frank FC (1966) Deduction of earth strains from survey data. Bull Seismol Soc Am 56:35–42
Fredlund DG, Krahn J (1977) Comparison of slope stability methods of analysis. Can Geotech J 14:429–439. https://doi.org/10.1139/t77-045
Froude MJ, Petley DN (2018) Global fatal landslide occurrence from 2004 to 2016. Nat Hazards Earth Syst Sci 18:2161–2181. https://doi.org/10.5194/NHESS-18-2161-2018
Guerriero L, Bertello L, Cardozo N et al (2017) Unsteady sediment discharge in earth flows: a case study from the Mount Pizzuto earth flow, southern Italy. Geomorphology 295:260–284. https://doi.org/10.1016/j.geomorph.2017.07.011
Haneberg WC (2007) Directional roughness profiles from three-dimensional photogrammetric or laser scanner point clouds. In: ARMA Canada-US Rock Mechanics Symposium. ARMA
Haneberg WC (2008) Elevation errors in a LIDAR digital elevation model of West Seattle and their effects on slope-stability calculations. In: Baum RL, Godt JW, Highland LM (eds) Landslides and Engineering Geology of the Seattle, Washington, Area. Geological Society of America, pp 55–65
Haneberg WC, Gökce AO (1994) Rapid water-level fluctuations in a thin colluvium landslide west of Cincinnati, Ohio
Hungr O, Fell R, Couture R, Eberhardt E (2005) Landslide risk management. Taylor and Francis
Johnson SE, Haneberg WC, Bryson LS, Crawford MM (2023) Measuring ground surface elevation changes in a slow-moving colluvial landslide using combinations of regional airborne lidar, UAV lidar, and UAV photogrammetric surveys. Q J Eng Geol Hydrogeol. https://doi.org/10.1144/qjegh2022-078
Keaton JR, Gailing RW (2004) Monitoring slope deformation with quadrilaterals for pipeline risk management. In: 2004 International Pipeline Conference, vol 41766. ASMEDC, Calgary, pp 269–274
Khabiri S, Crawford MM, Koch HJ et al (2023) An assessment of negative samples and model structures in landslide susceptibility characterization based on Bayesian network models. Remote Sens 15:3200. https://doi.org/10.3390/rs15123200
Kirschbaum DB, Adler R, Hong Y et al (2010) A global landslide catalog for hazard applications: method, results, and limitations. Nat Hazards 52:561–575. https://doi.org/10.1007/s11069-009-9401-4
Koralegedara NH, Maynard JB (2017) Chemical, mineralogical and textural properties of the Kope Formation mudstones: how they affect its durability. Eng Geol 228:312–322. https://doi.org/10.1016/j.enggeo.2017.08.025
Leprince S, Barbot S, Ayoub F, Avouac J-P (2007) Automatic and precise orthorectification, coregistration, and subpixel correlation of satellite images, application to ground deformation measurements. IEEE Trans Geosci Remote Sens 45:1529–1558. https://doi.org/10.1109/TGRS.2006.888937
Malet J-P, Maquaire O, Calais E (2002) The use of Global Positioning System techniques for the continuous monitoring of landslides: application to the Super-Sauze earthflow (Alpes-de-Haute-Provence, France). Geomorphology 43:33–54. https://doi.org/10.1016/S0169-555X(01)00098-8
Marmoni GM, Martino S, Censi M et al (2023) Transition from rock mass creep to progressive failure for rockslide initiation at Mt. Conero (Italy). Geomorphology 437:108750. https://doi.org/10.1016/j.geomorph.2023.108750
Mazza D, Cosentino A, Romeo S et al (2023) Remote sensing monitoring of the Pietrafitta earth flows in Southern Italy: an integrated approach based on multi-sensor data. Remote Sens 15:1138. https://doi.org/10.3390/rs15041138
Medina-Cetina Z, Song A, Zhu Y et al (2022) Global and local deformation effects of dry vacuum-consolidated triaxial compression tests on sand specimens: making a database available for the calibration and development of forward models. Materials 15:1528. https://doi.org/10.3390/ma15041528
Mirus BB, Jones ES, Baum RL et al (2020) Landslides across the USA: occurrence, susceptibility, and data limitations. Landslides 17:2271–2285. https://doi.org/10.1007/s10346-020-01424-4
Morcioni A, Apuani T, Cecinato F (2022) The role of temperature in the stress–strain evolution of alpine rock-slopes: thermo-mechanical modelling of the Cimaganda rockslide. Rock Mech Rock Eng 55:2149–2172. https://doi.org/10.1007/s00603-022-02786-y
Okyay U, Telling J, Glennie CL, Dietrich WE (2019) Airborne lidar change detection: an overview of Earth sciences applications. Earth-Sci Rev 198:102929. https://doi.org/10.1016/j.earscirev.2019.102929
Pietrantonio G, Riguzzi F (2004) Three-dimensional strain tensor estimation by GPS observations: methodological aspects and geophysical applications. J Geodyn 38:1–18. https://doi.org/10.1016/j.jog.2004.02.021
Qin R, Tian J, Reinartz P (2016) 3D change detection – approaches and applications. ISPRS J Photogramm Remote Sens 122:41–56. https://doi.org/10.1016/j.isprsjprs.2016.09.013
Schulz WH, Coe JA, Ricci PP et al (2017) Landslide kinematics and their potential controls from hourly to decadal timescales: insights from integrating ground-based InSAR measurements with structural maps and long-term monitoring data. Geomorphology 285:121–136. https://doi.org/10.1016/j.geomorph.2017.02.011
Shen Z-K, Jackson DD, Ge BX (1996) Crustal deformation across and beyond the Los Angeles basin from geodetic measurements. J Geophys Res Solid Earth 101:27957–27980

Teza G, Pesci A, Genevois R, Galgaro A (2008) Characterization of landslide ground surface kinematics from terrestrial laser scanning and strain field computation. Geomorphology 97:424–437
Varnes DJ (1978) Slope movement types and processes. In: Schuster RL, Krizek RJ (eds) Landslides, Analysis and Control. National Academy of Sciences, pp 11–33
Zhu Y, Medina-Cetina Z (2022) Assessment of spatio-temporal kinematic phenomena observed along the boundary of triaxial sand specimens. Appl Sci 12:8091
Zhu Y, Dortch JM, Massey MA et al (2021) An intelligent swath tool to characterize complex topographic features: theory and application in the Teton Range, Licking River, and Olympus Mons. Geomorphology 387:107778. https://doi.org/10.1016/j.geomorph.2021.107778
Zhu Y, Medina-Cetina Z, Pineda-Contreras AR (2022) Spatio-temporal statistical characterization of boundary kinematic phenomena of triaxial sand specimens. Materials 15:2189
Zhu Y, Medina-Cetina Z, Wang C, Bi X (2026) Three-dimensional dynamics of vortex structures in granular materials. Powder Technol 471:122081. https://doi.org/10.1016/j.powtec.2025.122081
Zienkiewicz OC (1971) The finite element method in engineering science. McGraw-Hill, London, New York

Sarah Johnson
Department of Earth and Environmental Sciences, University of Kentucky, Lexington, KY 40506-0107, USA

Yichuan Zhu (✉)
Department of Civil & Environmental Engineering, Temple University, 1947 N. 12, Room 524, Philadelphia, PA 19122-6018, USA
Email: yichuan.zhu@temple.edu

Jason M. Dortch
Kentucky Geological Survey, University of Kentucky, Lexington, KY 40506-0107, USA

William C. Haneberg
Geologic and Geohazards Consultant, Albuquerque, NM 87120-7407, USA